Fatigue damage mechanisms and damage evolution near cyclically loaded edges

R. EBNER[1,*], P. GRUBER[1], W. ECKER[1], O. KOLEDNIK[2], M. KROBATH[1], and G. JESNER[3]

[1] Materials Center Leoben Forschung GmbH, Roseggerstrasse 12, 8700 Leoben, Austria
[2] Erich Schmid Institute of Materials Science, Austrian Academy of Sciences, Jahnstrasse 12, 8700 Leoben, Austria
[3] Böhler Edelstahl GmbH & Co KG, Kapfenberg, Austria

Abstract. A combined experimental and numerical approach was applied to develop a basic understanding of the fatigue damage process taking place at edges exposed to cyclic mechanical loads.

A recently developed cyclic edge-loading test was used in order to simulate the fatigue loading of the edges of manufacturing tools and to study the microscopic damage mechanisms. Accompanying finite element calculations were performed to provide a better understanding of the loading conditions at edges subjected to cyclic mechanical loads. A comparison of the numerical simulation with the experimental results revealed good accordance.

Main results of the investigations are the distribution of plastic strains and their evolution with increasing number of cycles, the distribution of the residual stresses, the localisation and the evolution of damage at the microscale (microcracks and voids), and the localisation and growth of fatigue cracks.

Micro-damage develops in the entire plastically deformed region. Fatigue crack nucleation was mainly found in deformation bands and fatigue crack growth was only observed near the transition region between the extensively and the slightly plastically deformed zone not at the loaded area but at the side area. The reason for that phenomenon is the formation of tensile residual stresses in this region which is favouring fatigue crack growth.

Key words: fatigue damage, crack nucleation, plastic strains, residual stress.

1. Introduction

Failure of edges due to cyclic mechanical loading plays an important lifetime-controlling role in various technological fields. Examples range from tools with a wide range of shapes and sizes used in various manufacturing processes to edges of structural components or rail heads [1–4].

Edges may be exposed to very complex loading conditions in which not only the load amplitude varies but also the loading direction. Despite this fact many cyclically loaded edges show a characteristic failure appearance. Cracking mainly does not occur at that surface, at which the main load is applied, but at the other surface [5, 6]. E.g. in punching tools, the crack initiation and crack growth often does not occur at the end face but at the side area. Crack initiation and crack growth mainly takes place in a specific distance from the loaded edge [5]. In a later stage of the damage process these fatigue cracks may cause breaking away of chips from the cutting edge, causing the end of the tool life. Similar kind of damage may be observed also in rail heads subjected to local overloads caused by rolling contact fatigue [7]. Mechanical loading of edges causes very specific and inhomogeneous stress and strain fields with high gradients [8]. In the region, where the main fatigue damage occurs, fatigue loading takes place with high compressive mean stresses [5, 9].

Damage is a term that is often used but not consistently defined. Materials scientists often understand damage as a process that starts with the very first softening of the material at the micro- or nanometer scale and that proceeds with the nucleation of microcracks that subsequently grow to form larger cracks and to cause finally the failure of the component [10]. Mechanical engineers consider damage as a meso-scale effect where material separation is detected at a coarser scale, e.g. by radiography or ultrasonics techniques. In this paper, the fatigue damage process of edges is considered from the materials scientists' point of view.

Damage normally starts with pre-steps which do not directly form microcracks but have a significant influence on the formation of such microcracks. The development of strain localisations and residual stresses are among the most important damage relevant pre-steps in the fatigue process [11, 12]. These fatigue relevant pre-steps are experimentally accessible only with highly sophisticated techniques such as electron optical or synchrotron radiation based diffraction techniques [6, 13]. Microcracks with a typical size in the micrometer or even sub-micrometer range are normally formed by decohesion of interfaces or by failure of hard and brittle particles [14]. These microcracks may act as starters for subsequent fatigue crack growth. Growth of such small cracks differs significantly from that of the classical long cracks [15]. Differences can be expected mainly due to reduced crack closure effects, caused by the small crack size but also due to growth of cracks in a material which is subjected to plastic strain cycles.

*e-mail: reinhold.ebner@mcl.at

R. Ebner, P. Gruber, W. Ecker, O. Kolednik, M. Krobath, and G. Jesner

At cyclically loaded edges the fatigue process takes place with high compressive mean stresses. It is well known from literature that a compressive mean stress reduces microcrack nucleation and growth [16] but fatigue failure is frequently observed in highly loaded edges. It is argued that the fatigue process of cyclically loaded edges is strongly related to residual stresses that are formed if local plastic deformation occurs in inhomogeneous stress fields [17]. This effect is well known from other fields, e.g. from thermally cycled surfaces in pressure die casting moulds [18] or from fatigue loading of notched specimens [19].

In order to avoid fatigue damage at cyclically loaded edges and for the development of materials with improved resistance to fatigue failure of edges, it is of great relevance to understand the damage mechanisms and the damage evolution from the very first beginning till the end of life.

2. Methodological approach

A combined experimental and numerical approach was applied to develop a basic understanding of the fatigue damage process taking place at edges exposed to mainly compressive cyclic mechanical loads.

2.1. Physical simulation of edge loading. A specific cyclic edge-loading test was developed recently in order to investigate the microscopic damage phenomena at the loaded edges of tools and to study the nucleation and growth of cracks. The principle of the edge-loading test is shown in Fig. 1.

Loading was performed by means of a cylinder with 12 mm diameter made of hard metal. This cylinder was cyclically pressed onto the edges of two rectangular prisms which were precisely fixed in a well defined distance to each other. The prisms made of the investigated tool steel had a thickness of 5 mm, a height of 10 mm, and a length of 15 mm.

One of the rectangular prisms was made of two parts (split-specimen), similar to the procedure applied in [20]. The cut surface of the split-specimen was ground and mechanically polished with procedures similar to metallographic sample preparation. This preparation is required for determining plastic strain distributions near the loaded edges by comparing scanning electron microscopy (SEM) micrographs from this region before and after loading or after different loading cycles [21–24].

In order to study the effect of cyclic loading, the specimens were mounted in a stiff loading device. The distance between the prisms was fixed by means of a distance plate. Clamping was performed by means of screws in x and z direction positioned at the lower part of the prisms. The clamping forces need to be high enough to constrain the prisms in x- and z-direction.

A high precision clamping device was used in order to guarantee that test specimens can be removed and remounted several times in order to study the effect of fatigue loading after different numbers of cycles. Investigating the strain fields was limited roughly to about 150 cycles because the interaction (friction) between the surfaces and the related surface

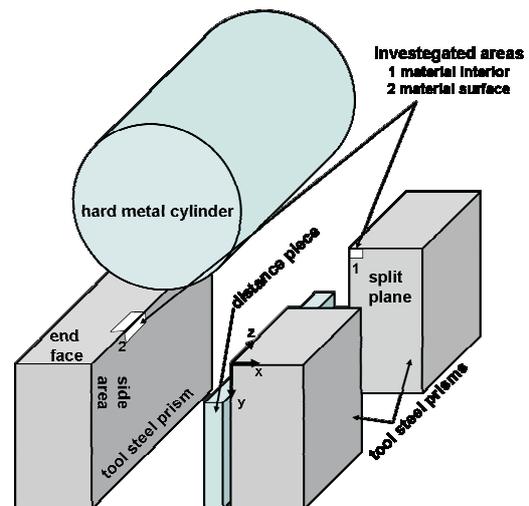degradation of the split specimen made strain analyses impossible.

a)
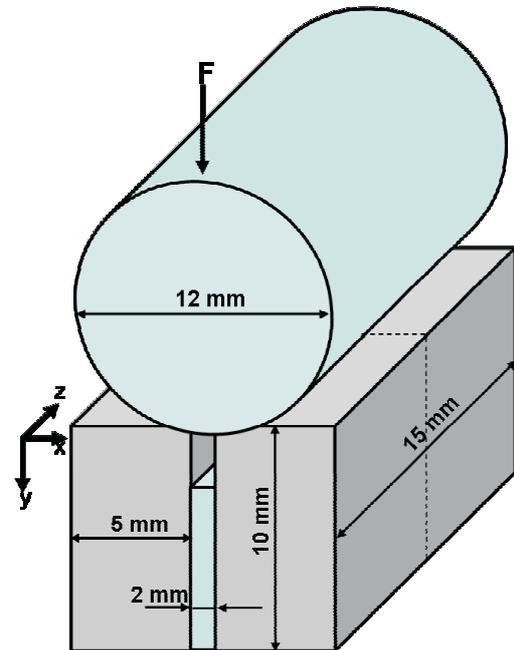
b)

Fig. 1. a) Test set up; b) Exploded view

Cyclic mechanical testing was performed on a servo hydraulic testing machine at frequencies up to about 1 Hz. The maximum compressive loads were chosen in the range of 5 and 90 kN. Two types of cyclic tests were performed: In test type 1 the loads were varied between the maximum compressive load (F_{min}) and 0 kN ($F_{1,max}$), in test type 2 the loads were varied between the maximum compressive load (F_{min}) and 10% of this maximum load ($F_{2,max}$).

The specimens were alternately subjected to a predefined number of load cycles and afterwards inspected with respect to shape changes, strain distribution, micro-damage and cracks. The following information was determined from the specimens outlined in Fig. 1:

- Shape changes of specimens after loading were characterised at the end face and the side area by means of confocal laser scanning microscopy.
- Strain distribution near the edge was determined at the split plane by comparing SEM images from this region before and after loading.
- Surface roughness was determined at the side area by means of 3D surface analysis based on stereographic SEM images and from atomic force measurements.
- Microscopic damage and crack growth were determined from metallographic sections taken from the x-y plane.

2.2. Material. The specimens for the edge-loading test were made of the powder metallurgy high speed tool steel S390 MICROCLEAN from Böhler Edelstahl GmbH & Co KG; the chemical composition of the steel is summarised in Table 1. Manufacturing of the specimens comprised of the following steps: (1) Pre-machining, (2) hardening in vacuum furnace using high pressure nitrogen gas quenching, (3) multiple tempering to achieve a hardness of 62 HRC, (4) grinding, (5) polishing.

Table 1

Chemical composition of the high speed tool steel S390 MICROCLEAN in weight percent

Steel grade	C	Cr	Mo	V	W	Co	Balance
Böhler S390 MICROCLEAN	1.64	4.80	2.00	4.80	10.40	8.00	Fe

Figure 2 shows a SEM micrograph of the microstructure. Two types of primary carbides are visible, white M_6C and grey MC carbides, both have an average size of roughly 1 μm.
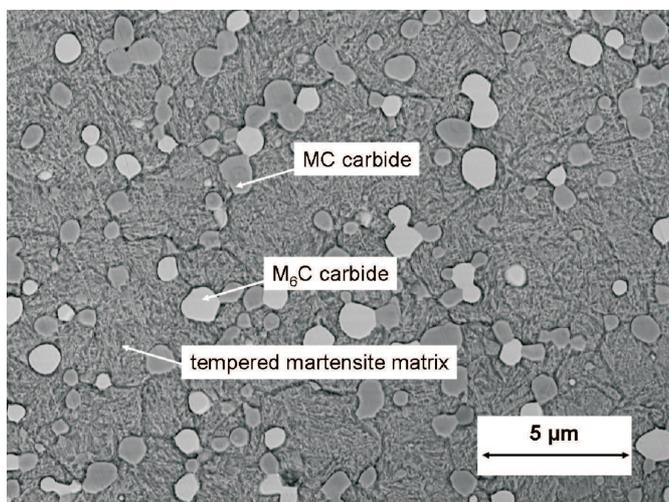

Fig. 2. Microstructure of the PM-tool steel grade S390 MICRO-CLEAN

The microstructure of the heat treated material consists of primary carbides embedded in a metallic matrix consisting of tempered martensite hardened by means of secondary hardening carbides. The volume fraction of the primary carbides is about 13%, that of the secondary hardening carbides is about 9% (estimated by means of Thermocalc ®).

The mechanical behaviour of the tool steel as determined by means of uniaxial compression tests is summarised in Table 2. Details of the stress-strain behaviour of the high speed steel in case of compressive loading can be taken from Fig. 3. Exceeding the elastic limit, which is about 2000 MPa, the material shows strong strain hardening up to a strain of about 2%, whereas the material shows almost ideal plastic behaviour at strains higher than 2%.

Table 2

Mechanical properties of the investigated PM high speed steel S390 MICROCLEAN as determined from compression tests

$R_{p0.05}$ [MPa]	$R_{p0.2}$ [MPa]	R_m^* [MPa]	E [MPa]
2.140	2.950	3.140	219.000

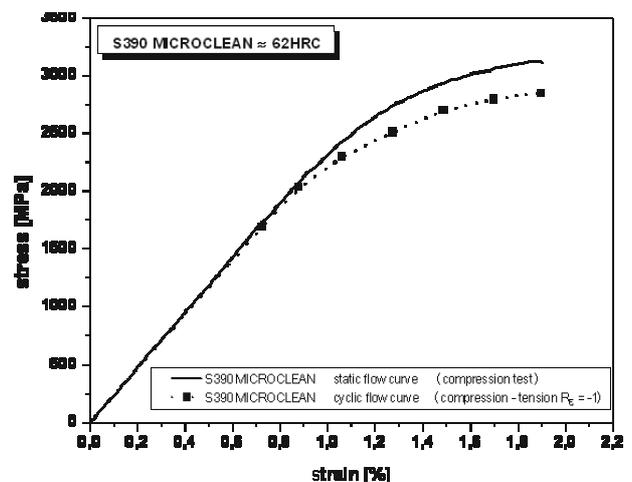* Maximum stress achieved in the compression test

Fig. 3. Stress-strain behaviour of the high speed steel S390 MICRO-CLEAN

Total strain-controlled cyclic experiments were performed in order to determine the cyclic stress-strain behaviour. The cyclic stress-strain curve was determined from compression-tension tests taking the stress and strain amplitudes found in the stable hysteresis loop at 50% of the number of cycles to failure ($N_f/2$). The cyclic stress-strain curve is shown in Fig. 3 together with the stress-strain curve determined in static tests. It is evident from Fig. 3 that the steel shows roughly 10% cyclic softening, but it has to be pointed out that this cyclic softening is significantly affected by the tension-compression asymmetry of the tool steel. The static stress strain curve in Fig. 3 was determined from a compression test, the cyclic stress-strain curve was determined from a compression-tension test with a strain ratio $R_\varepsilon = 1$. The stress and strain values of the cyclic stress-strain curve were determined from the stress range and the total strain range by dividing these experimentally determined values by a factor of two.

2.3. Residual stress measurement. Residual stress measurements were performed by means of a commercial X-ray diffraction system, Fig. 4. The residual stresses were determined from the lattice strains based on the widely used the $\sin^2 \psi$

method [25]. The measurements were performed with Cr K_α radiation with a beam diameter of approximately 800 μm. In order to get a rough estimation of the residual stress distribution near the loaded edge, residual stress measurements were performed along the side area in steps of 100 μm starting at deformed edge after loading. Due to the residual stress gradient near the plastically deformed edge it can be assumed that the measured residual stresses are weighted mean values from the residual stress distribution within the analysed circular surface.
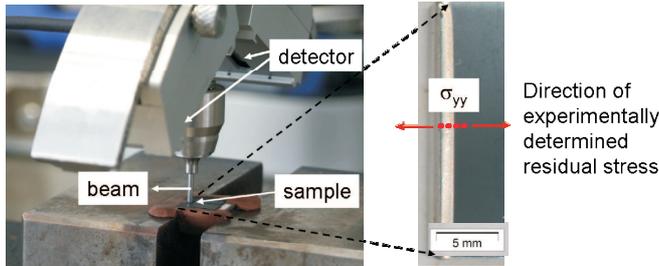
Fig. 4. X-ray based determination of residual stresses at loaded edges

2.4. Numerical simulation. A goal of the finite element simulations was the prediction of the stress and strain evolution in the edge-loading test near the loaded edge during static and cyclic loading.

A finite element simulation model was developed based on the commercial software package ABAQUS [26] to perform these calculations. Due to symmetry reasons only half of the experimental setup is modelled in a 2D model assuming plane strain conditions in z-direction. The load is applied onto a rigid punch which is in frictionless contact with the top of the hard metal roll. The boundary conditions are chosen as indicated in Fig. 5. The bottom plane is constrained in y-direction and the vertical plane is constrained in x-direction.
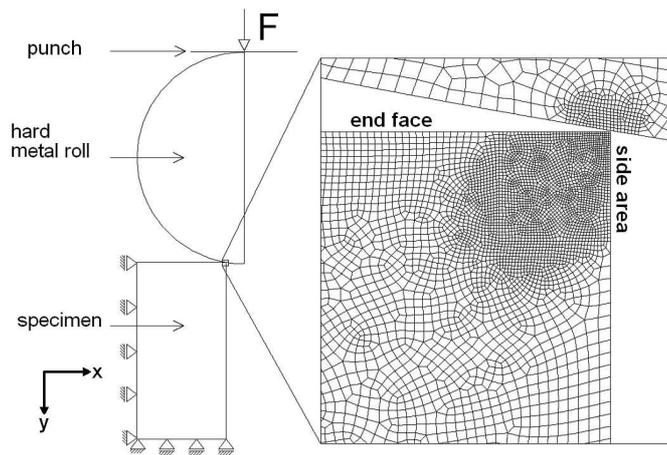

Fig. 5. Finite element model of the edge loading test

The contact between the hard metal cylinder and the specimen is modelled using a friction coefficient of 0.1. The material behaviour of the hard metal cylinder is assumed to be elastic. The elastic-plastic material behaviour for the first loading

and unloading of the S390 specimen is described by the stress-strain curve determined from a compression test by a simple form of a Chaboche-type model including two nonlinear kinematic hardening terms [27, 28]. In order to model the cyclic softening of the material in subsequent loading-unloading cycles the material parameters are modified to match the cyclic stress strain curve of cycle 5 and 25 of a uniaxial compression-tension tests. The equations describing the material behaviour are summarized in Fig. 6a and the stress strain behaviour for cycle 1, 5 and 25 is depicted in Fig. 6b.
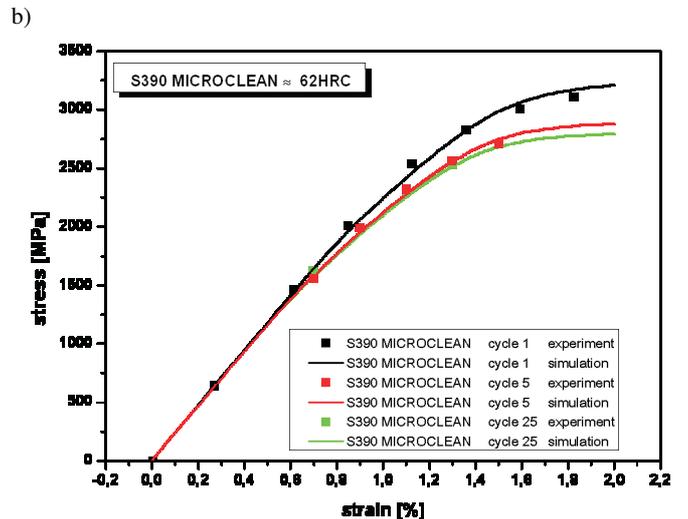
a)

b)

Fig. 6. Summary of the material model: a) model equations, b) comparison of uniaxial stress strain behaviour of experimental data and numerical results

The local loading near the edge of a sample tested in the edge-loading test reaches a level which is far beyond the limit of the loading level of uniaxial tests, but assuming almost ideal plastic material behaviour for plastic strains higher than 2% seems to be an appropriate assumption for the high loading regime.

3. Results

3.1. Shape changes. Loading the edge with the hard metal cylinder causes typical shape changes of the edge, Fig. 7. During compression loading the hard metal cylinder is pressed into the end face and material moves out from the side area due to plastic deformation. The shape changes were determined at specimens after 5 loading-unloading cycles. This procedure was chosen to avoid influences from friction which is ex-

pected to be most likely in the first cycle because the largest relative movement between the hard metal cylinder and the specimen mainly takes place in this cycle.
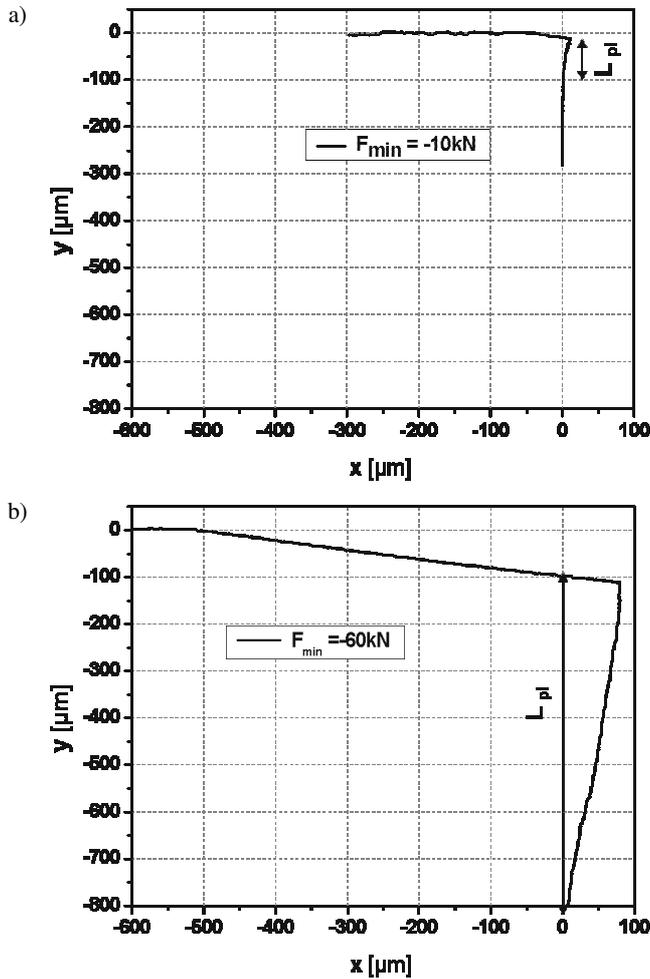

a)

b)

Fig. 7. Shape change due to the local edge loading after 5 loading-unloading cycles (view onto the x-y plane defined in Fig. 1): a) Edge profile after loading to 10 kN, b) Edge profile after loading to 60 kN

After unloading the shape changes were characterised by means of confocal laser scanning microscopy which was used to determine surface profiles and by means of metallographic sections. Figures 7a and 7b show the typical edge shape of a specimen after loading to 10 and 60 kN respectively. There are two zones: Zone I is located directly at and below the loaded edge and is characterised by high plastic strains and a significant shape change. The extension of zone I is marked by the length L_{pl} at the side area. Zone II is located at the side area below zone I and is characterised by only small shape changes but this zone II is still plastically deformed.

The extension of the extensively deformed zone I with significant shape change L_{pl} is about 100 μm in case of 10 kN loading and about 600 μm in case of 60 kN loading. Detailed analyses of the relationship between the compression load F and the size of the extensively deformed zone I at the side area L_{pl} revealed an almost linear relationship, Fig. 8. Figure 8 also indicates a good accordance between the exper-

imentally found and the simulated values of the size L_{pl} of the extensively deformed zone I if 2% plastic strain is taken as boundary of the extensively deformed region in the finite element simulations.
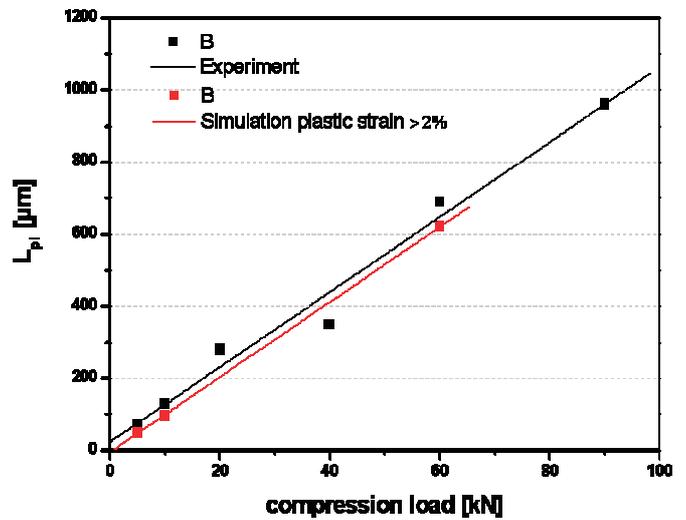

Fig. 8. Experimentally determined and numerically simulated size L_{pl} of the extensively plastically deformed zone I at the side area after 5 load cycles as a function of the maximum compressive load (plastic strain criterion for the boundary of the extensively plastically deformed zone predicted in the finite element simulation: 2%)

Figure 9 shows for selected points the experimentally determined displacement vector field for an edge exposed to a compression load of 5 kN. The displacement vector field reveals that the material flow at the edge primarily takes place in the loading direction (top to bottom) and out of the side area (left to right). The maximum displacement occurs at the edge and is in the range of about 8 μm at the edge and the size L_{pl} of the extensively plastically deformed zone with pronounced shape changes is about 60 μm.
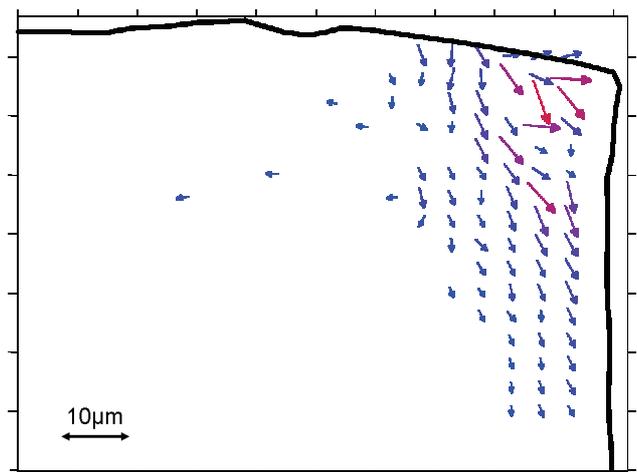

Fig. 9. Displacement vector field in the x-y plane after compression loading of the edge up to 5 kN visualised for selected points

The complete displacement vector field can only be determined for lower loads up to about 10 kN. At higher loads

the displacements and the strains are too large for the applied measurement technique leading especially near the edge to areas that cannot be analysed quantitatively.

3.2. Strain fields. The strain field was determined from the split plane by comparing SEM micrographs of the edge region on the split plane before and after loading via digital image analysis [22]. Again, the entire plastically deformed zone can be characterised only for loads up to about 10 kN. The strains prevalent in case of edges exposed to higher loads exceed the maximum detectable strain.
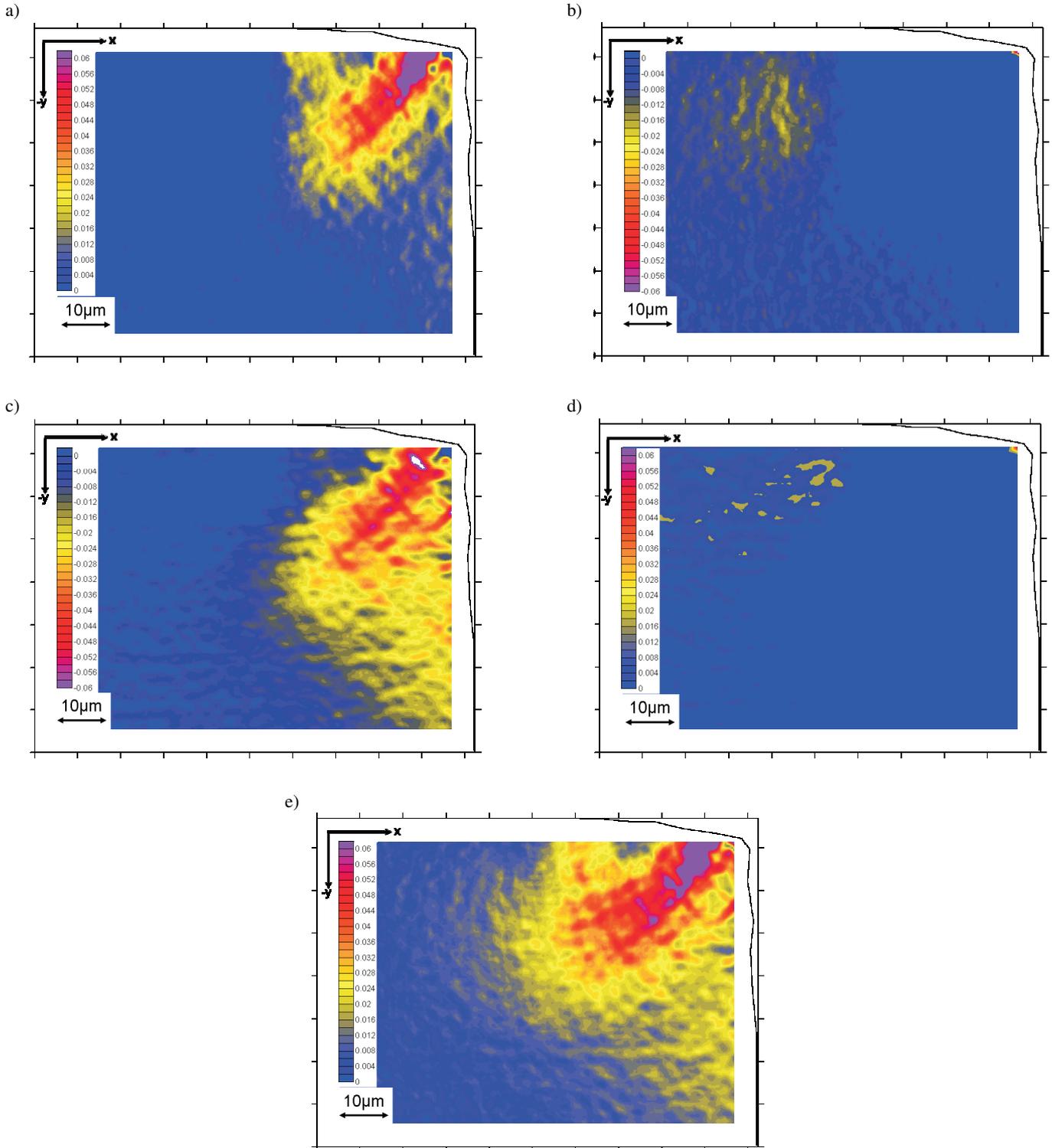

Fig. 10. Plastic strain determined from SEM micrographs of the edge region of the split specimen after one load cycle to 5 kN: a) positive strain in x-direction, b) negative strain in x-direction, c) negative strain in y-direction, d) positive strain y-direction, e) equivalent strain

Fatigue damage mechanisms and damage evolution near cyclically loaded edges

Figure 10 shows details about the plastic strain distribution in the split plane (x-y plane) after one load cycle to 5 kN. The strains in x-direction are positive directly below the hard metal cylinder with maximum values up to about 6%, Fig. 10a, and negative in the neighbouring region with maximum values of about 2%, Fig. 10b. Figure 10a indicates that there exists a deformation band oriented about $45°$ to the loading direction with maximum strain values directly at the edge. The strains in y-direction are negative directly below the hard metal cylinder again with maximum values up to about 6%, Fig. 10c, and positive in the neighbouring region with maximum values of about 2%, Fig. 10d. The deformation band with strain values up to about 6% is also visible in Fig. 10c. In Fig. 10e the distribution of the equivalent strain is shown. Figure 10e indicates two regions with higher plastic strains. One of these regions is the deformation band which originates at the edge and penetrates the material at an angle of about $45°$ inclined to the loading direction; the second region has the shape of a quadrant with its centre at the edge. This second high-strain zone is formed at the transition region of the extensively plastically deformed contact area between the hard metal cylinder and the tool steel sample and penetrates the entire edge region from the end face to the side area.

Apart from the meso-scale pattern described above, the strain distribution images further reveal that at the microscopic scale the strain is inhomogeneously distributed within the material. Such an inhomogeneous deformation pattern at the microscopic scale was also reported in [24] for metal matrix composites and for the pure matrix material. Local strain maxima can be found in all plastically deformed regions. In the low strain regions the strain maxima are in the range of about 2% whereas the surrounding strain minima are not detectable and thus perhaps zero. In the higher strain areas strain maxima of about 6% can be found embedded in areas with strain minima of about 2%. The spacing of the strain maxima/minima is about 6 μm which is almost equal to the spacing of the primary carbides.

The equivalent plastic strain map in Fig. 10e indicates that plastic strains higher than 2% are detectable up to a distance of about 50 μm from the edge in x-direction and up to about 60 μm in y-direction. It can be further concluded from Fig. 10e that the total plastically deformed region is much larger and in the range of about 150 μm.

Figure 11a shows the experimentally determined equivalent strain accumulated between the end of the first and the end of the 5th load cycle and Fig. 11b between the end of the 5th and the end of the 25th load cycle. These results indicate extensive plastic straining in the first cycles which strongly decay with increasing number of cycles.

During cycles 2 and 5 plastic straining concentrates in the high strain regions which were already present after the first loading-unloading cycle. Highest strains in the range up to about 6% occur in the quadrant-shaped plastic zone that encompasses the higher strain region from the lower strain region and in the deformation band formed at the edge. During cycles 6 and 25 further plastic straining is observed but it

takes place localised in very narrow zones. In these hot spots plastic strains exceed a level of about 1%. Detailed studies up to about 150 cycles revealed that plastic straining slows down with increasing numbers of cycles indicating that elastic shake down occurs.
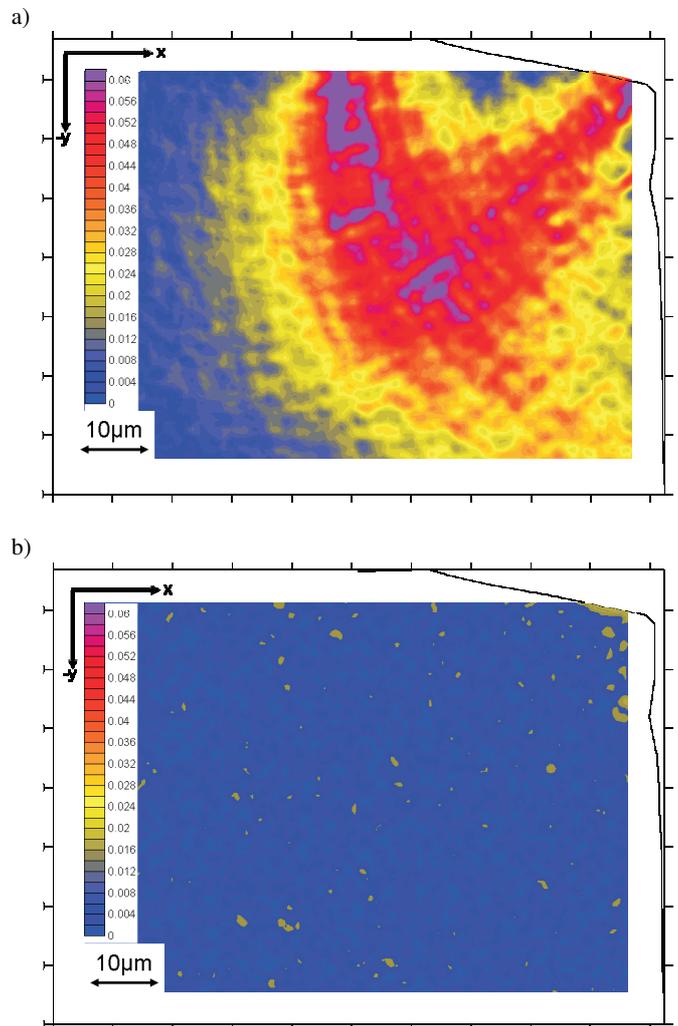
a)

b)

Fig. 11. Equivalent plastic strain determined from SEM micrographs of the edge region after loading with 5 kN: a) plastic strain accumulated during load cycle 2 and 5; b) plastic strain accumulated during load cycle 5 and 25

Cyclic plastic straining of materials causes microstructural changes which are connected with an alteration of the mechanical properties. The investigated tool steel S390 shows cyclic softening similar to many metallic materials with a high hardness. In order to study the effect of cyclic softening on the strain distribution finite element calculations were performed. For simplification, only three load cycles were simulated but assuming that the flow curve is the cyclic stress strain curve at the cycles 1, 5 and 25, Fig. 6b. Figure 12a shows the calculated plastic strain accumulated during the second simulated load cycle, which can according to the cyclic softening assumptions be compared with the plastic strain accumulated during cycles 2 to 5 in the experiment in Fig. 11a. In the

R. Ebner, P. Gruber, W. Ecker, O. Kolednik, M. Krobath, and G. Jesner

simulation and in the experiment two regions of high straining occur. One region is a deformation band originating at the edge and reaching under an angle of 45° about 50 μm into the specimen. The location of this deformation band is similar in simulation and experiment, but in the simulation the lateral extension of the highly strained region is smaller. The second region of high strain is located near the 2% strain iso-line of the first cycle. Again the location of this region is similar in simulation and experiment, but near the end face in the simulation the deformation band appears to be almost linear under an angle of 45° which is in contrast to the curved shape in the experiment.
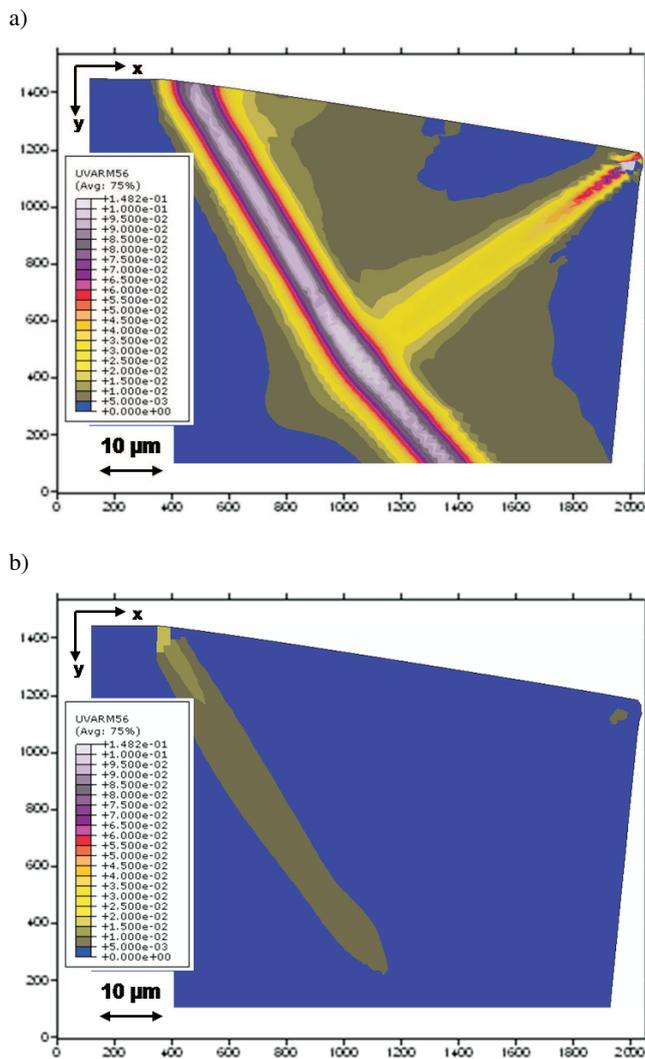
a)

b)

Fig. 12. Equivalent plastic strain distribution after loading with 10 kN determined by means of finite element calculations: a) distribution of equivalent plastic strain accumulated during load cycles 2 and 5; b) distribution of equivalent plastic strain accumulated during load cycles 6 and 25

Compared to the experiment the simulation gives too high strains and a too small deformation band width. The reason for these discrepancies lies in the fact that in the simulation model all the cyclic softening taking place during cycles 2 and 5 concentrates in one simulation cycle. Therefore the strain distribution determined in the experiment is a sum of the deformation bands of each cycle which forms in each cycle at a different position. This explains both the fact that the band width is too small in the simulation and the fact that the calculated strain within this band is too high. In Fig. 12b the simulated plastic strain accumulated between load cycles 6 and 25 is depicted. The overall picture is similar as experimentally observed, Fig. 11b, but again the strain is for the same reason as described above too much concentrated in the simulation.

The results clearly indicate strain localisations in the deformation band at the edge and in the quadrant-shaped zone that encompasses the higher strain region from the lower strain region. Calculations with a more sophisticated constitutive material model that considers combined isotropic and kinematic hardening revealed also inhomogeneous deformation in deformation bands, but the results are very sensitive to the material parameters and to the finite element mesh used and requires further investigations. Although final conclusions cannot be drawn at this point it can be assumed to be very likely that the strain localisations found between cycle 2 and 5 are mainly caused by cyclic softening of the tool steel.

3.3. Damage evolution. The evolution of damage near the cyclically loaded edge is summarised in Fig. 13a. Cracks and their orientation are marked with small bars and voids are marked with circles. Areas with similar damage pattern are encircled by drawn curves.

The experimental results reveal that different micro-damage processes take place at different positions after different numbers of cycles. After the first load cycle micro-damage occurs predominantly at position A at the side area near the transition to the elastically deformed region, Fig. 13b. Micro-damage takes place in form of microcracking of primary carbides which mainly occurs perpendicular to the load direction (y-direction). After five load cycles, remarkable additional microcracking of primary carbides is found at position B, Fig. 13c, and a few broken carbide clusters can be also found in the entire region with plastic strains higher than about 2%. The microcracks at position B are mainly oriented perpendicular to the load direction whereas cracking of carbide clusters in the rest of the plastically deformed zone seems to be statistically oriented. After 25 cycles increased microcracking of primary carbides parallel to the load direction is observed below the contact area between the steel sample and the hard metal cylinder. After 1,000 load cycles the number of microcracks and voids has significantly increased in a roughly 10 μm thick zone at the side area, Fig. 13d.

Up to 10,000 cycles no fatigue cracks were found in the entire plastically deformed region which have started growing from microcracks except one fatigue crack which is found at position A, Fig. 13a.
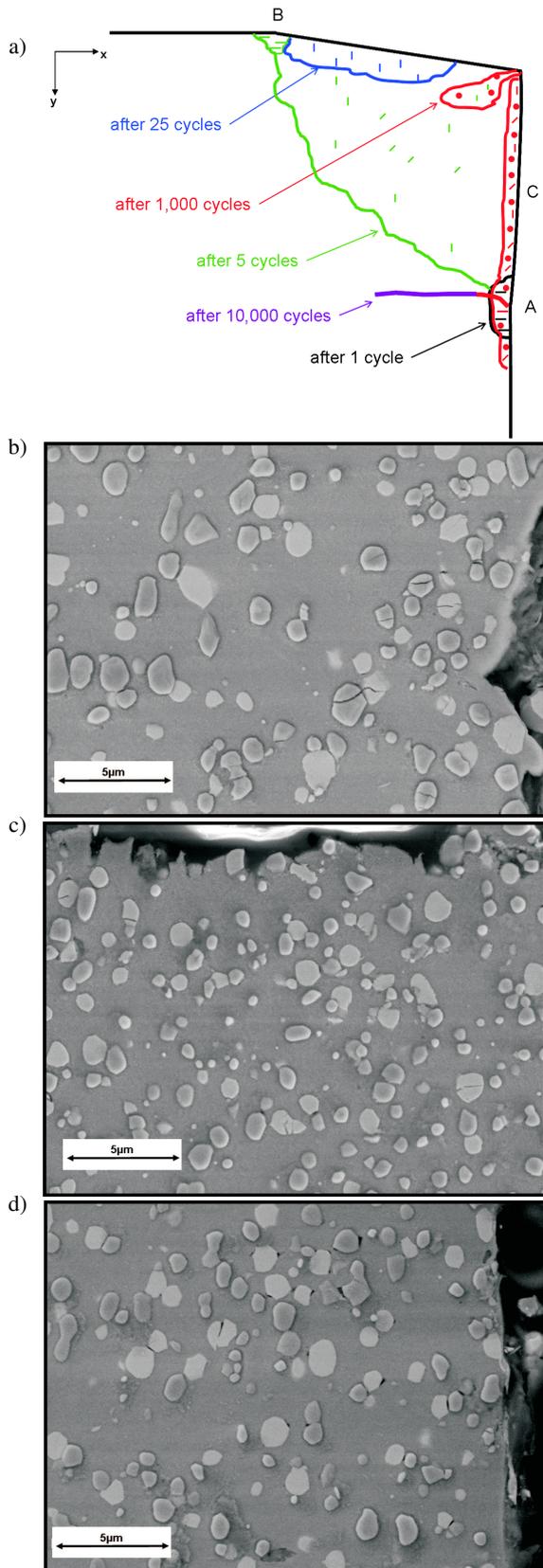
Fig. 13. Damage evolution at the cyclically loaded edge: a) schematic overview; b) carbide cracking after one cycle at position A; c) carbide cracking after five cycles at position B; d) carbide cracking and decohesion after 1,000 cycles at position C

Figure 14 shows a front view onto the side area. The upper part of Fig. 14a shows the contact area of the specimen and the hard metal cylinder, the mid part shows the extensively plastically deformed zone followed by the low plastically deformed zone and at the bottom the originally polished surface is seen. Fatigue crack nucleation and fatigue crack growth takes place at the side area in the plastically deformed zone near the transition to the elastically deformed region. Figure 14b shows this transition region with a higher magnification. The rough surface structure of the area above the crack clearly indicates a high number of deformation bands, the surface appearance below the crack is much smoother but there are still signs of plastic deformation. From the experimental investigations it can be concluded that the transition from the extensively deformed to the low deformed zone takes place at roughly 2% plastic strain.
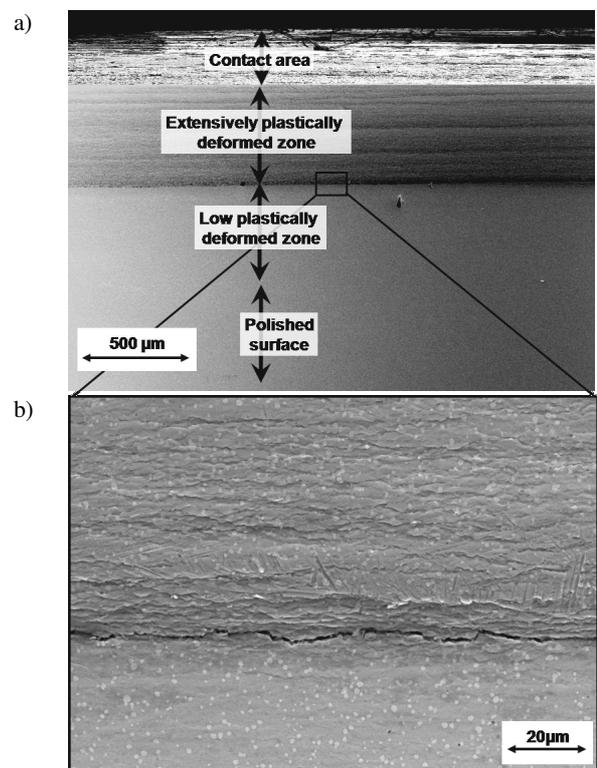

Fig. 14. Front view onto the side area in a specimen after loading to 60 kN after 10,000 cycles: a) overview; b) detail from a)

SEM and atomic force microscopy (AFM) investigations of the surface topography reveal a rough surface in the extensively plastically deformed zone.

Figure 15a shows a SEM micrograph of the side area after 125 load cycles to 10 kN. The surface which originally was polished now shows severe roughening comprising larger (L) and smaller (S) steps. Steps up to a few tenths of a micron were formed at the surface as indicated by the AFM profile shown in Fig. 15b. The spacing of the steps (appr. 6 μm) correlates well with the spacing of the local strain maxima in Fig. 9. It can thus be concluded that the deformation bands play a major role in the damage process, especially in crack nucleation.

R. Ebner, P. Gruber, W. Ecker, O. Kolednik, M. Krobath, and G. Jesner
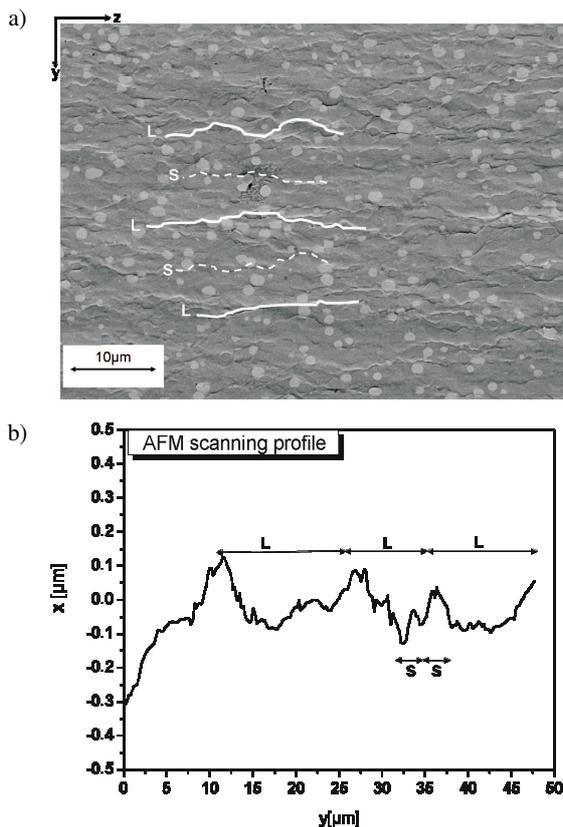
a)

b)

Fig. 15. Surface topography in the extensively plastically deformed zone: a) SEM micrograph after 125 load cycles; b) surface profile determined by means of atomic force microscopy
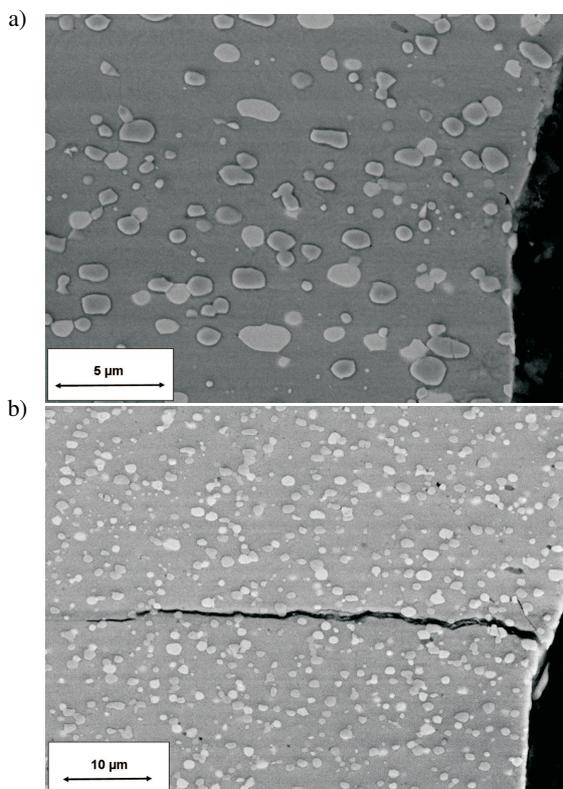
a)

b)

Fig. 16. Fatigue crack nucleation and propagation at position A after loading to 60 kN (different specimens): a) after 100 cycles; b) after 10,000 cycles

In order to study fatigue crack nucleation and fatigue crack growth metallographic sections were prepared from the transition region between the extensively and the low plastically strained zone, Fig. 16. Crack nucleation seems to occur very rapidly in deformation bands. A small crack with a depth of about 1 μm is visible in a deformation band already after 100 load cycles. The orientation of this crack nucleus directly at the surface is about 45 degrees inclined to the load direction, Fig. 16a. This leads to the conclusion, that such cracks are nucleated in shear bands. Such a shear band is also visible in Fig. 16b which was taken from a different specimen after 10,000 cycles. It is assumed that the microcracks formed in the carbides, as shown in Fig. 13b, may also act as fatigue crack nuclei. This leads to the conclusion that microcracking of carbides and microcrack formation in deformation bands are two competitive mechanisms that may form fatigue crack nuclei.

By comparing Fig. 14 and Fig. 16 it can be concluded that crack growth is much faster at the side area in z- and z-direction than into the depth (x-direction), e.g., the extension of the crack at the side area may be as large as several millimetres whereas the depth of the crack is still less than about 0.06 mm.

During crack growth into the depth, the orientation of the crack changes from the 45° orientation to a direction which is more perpendicular to the load direction, Fig. 16a and 16b. By comparing Fig. 16a and 16b the average crack growth rate can be estimated to be in the range of 5.10^{-6} mm/LW.

3.4. Conditions for crack growth. Finite element simulations were performed in order to study the local loading conditions.

Figure 17 shows the calculated distribution of the normal stress in y-direction σ_{yy} along the side area at different loading stages as a function of the distance from the edge. Curve 1 shows the stress distribution at maximum compression load, curve 2 after reduction of the load to 10% of the maximum compression load, and curve 3 after complete unloading.

The more or less constant maximum stress of about 3000 MPa at the maximum load (curve 1) is due to the assumption of an ideal plastic material behaviour for strains higher than 2%. In case of unloading to 10% of the maximum load (curve 2), the stresses remain compressive at any position of the side area. Tensile stresses at the side area can thus only be observed in case of an almost complete unloading. These findings are in agreement with the fact that no fatigue cracks were found in specimens which were unloaded only to 10% of the maximum load. The stress profile after complete unloading (curve 3) shows the residual stresses remaining in the specimen after the loading-unloading cycle.

It can be concluded from Fig. 17 that the maximum stress range is about 3200 MPa and that the maximum occurs at the transition region from the extensively to the low plastically deformed zone (region A in Fig. 13). Furthermore, the residual stress also reaches a maximum at this position. Both factors together promote fatigue crack growth and are suspected to be responsible for the existence of the fatigue crack

276

in this region. In all investigated specimens only very few cracks or even only a single fatigue crack could be observed. This phenomenon is expected to be caused by a shielding effect connected with a stress reduction in the areas near the crack.
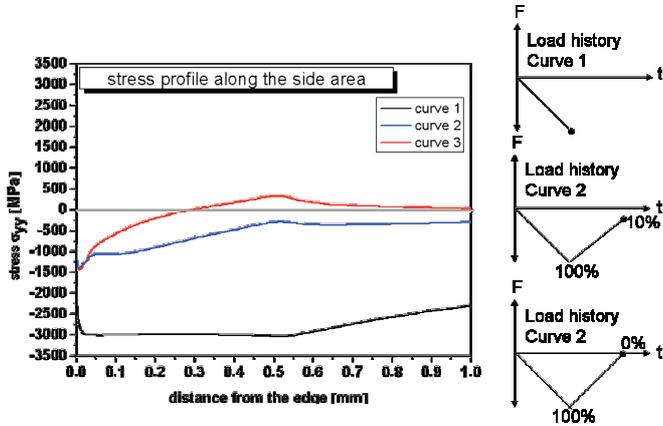

Fig. 17. Stress in y-direction along the side area as a function of the distance from the edge for an applied maximum load of 60 kN (curve 1), after unloading to 10% subsequent to applying the maximum load of 60 kN (curve 2), and after complete unloading subsequent to applying the maximum load of 60 kN (curve 3)

A rough estimation of the stress intensity factor range ΔK for the very small crack in the deformation band of about 1 μm length gives a value of about 3.5 MPa$\sqrt{m}$. Similar values can be estimated for the stress intensity factor ranges at the microcracks at broken carbides taking the typical size and the circular shape of these microcracks into account.

Due to the very small crack size and the fact, that the crack is growing in a cyclically plastic deformed material it can be assumed that there are almost no crack closure effects present and that the tip of the growing crack is thus fully exposed to the applied stress intensity factor range. Taking the threshold value for the effective intensity factor range ΔK_{eff} in steels 2.5 MPa$\sqrt{m}$ [11] it can be concluded that the crack tip loading of the 1 μm long crack shown in Fig. 14a is high enough to cause fatigue crack growth. The same conclusion can be drawn for microcracks in carbides shown in Fig. 13b.

Figure 18a and 18b show the calculated distribution of the residual stresses in y-direction σ_{yy}^{res} after compression loading to 10 and to 60 kN respectively followed by complete unloading. The residual stress in the y-direction σ_{yy}^{res} is considered because fatigue crack growth takes place perpendicular to this direction. Comparing Fig. 18a and 18b indicates that the stress patterns for loading to 10 kN and to 60 kN are very similar, only the size changes.

At the side area the residual stresses in y-direction σ_{yy}^{res} are compressive near the edge and the residual stresses change to tensile at the transition zone from the extensively to the low plastically deformed region. Such a maximum in tensile residual stresses was found for all simulated maximum loads in the transition region. The calculated residual tensile stresses in y-

direction σ_{yy}^{res} typically reach a maximum of about 200 MPa which is almost independent of the maximum load. The tensile stresses σ_{yy}^{res} reach into a depth of about 15 μm and about 100 μm in case of loading to 10 kN and 60 kN respectively and change than to compression. Fatigue crack growth studies indicate that fatigue cracks tend to slow down when they are approaching the depth where the residual stresses σ_{yy}^{res} change from tensile to compression. Fatigue cracks thus reach only a depth of about 10 μm in case of 10 kN maximum load and about 60 μm in case of 60 kN maximum load.
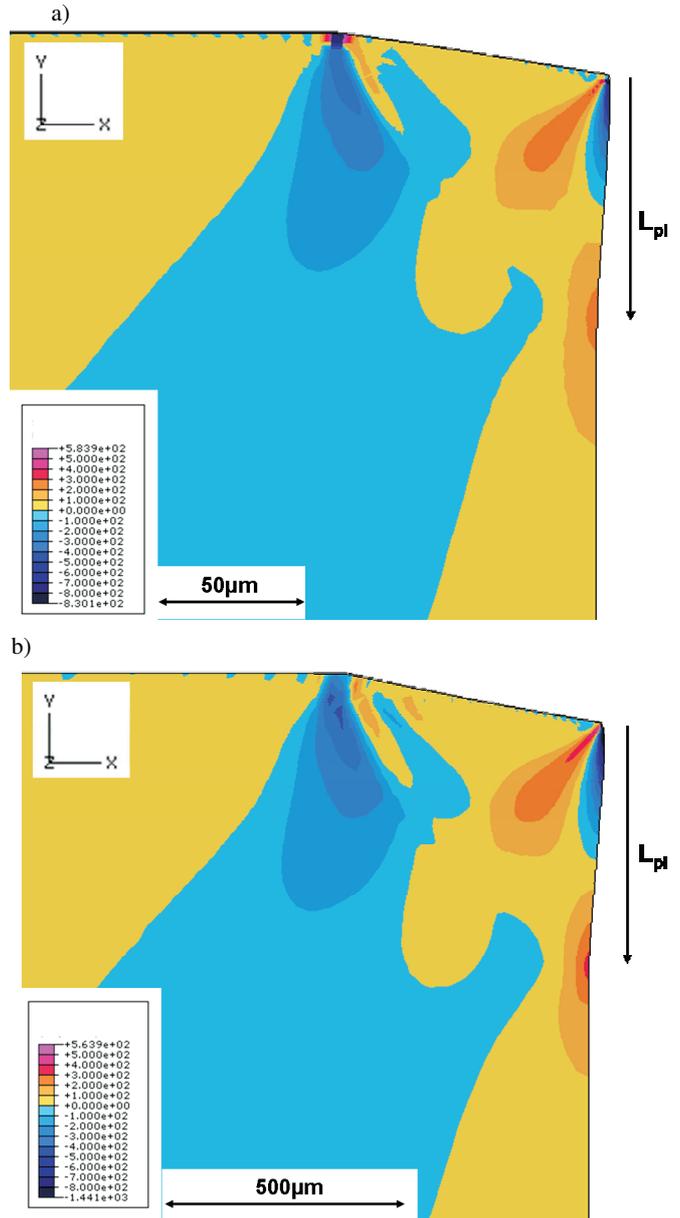

Fig. 18. Calculated distribution of residual stresses in y-direction σ_{yy}^{res} after a complete loading-unloading cycle: a) maximum compression load: 10 kN; b) maximum compression load: 60 kN

Experimental investigation of the residual stress distribution at the side area within the extensively deformed zone is a challenging task because of the small size of this zone. The

R. Ebner, P. Gruber, W. Ecker, O. Kolednik, M. Krobath, and G. Jesner

diameter of the used X-ray beam was about 0.8 mm which is large compared to the size of the plastically deformed zone. Therefore only mean values of the residual stress present in the analysed region could be determined.

The results of the residual stress measurements at the side area after a complete loading-unloading cycle with a maximum compression load of 60 kN are summarised in Fig. 19. The experimental results confirm the residual stress distribution from the finite element simulation. Starting with compressive residual stresses of about 400 MPa at the edge the residual stresses change to tensile and reach a maximum of about 200 MPa at a distance of about 0.6 mm from the edge. At larger distances from the edge the stresses decrease and approach a value of about -100 MPa far away from the edge. This low compression residual stress is due to polishing of the specimens prior testing. Taking the uncertainties in the used X-ray based residual stress measurement technique and the simplified cyclic material model used for the finite element calculations into account it can be concluded that the results from the experiments and the simulation are satisfyingly in accordance.
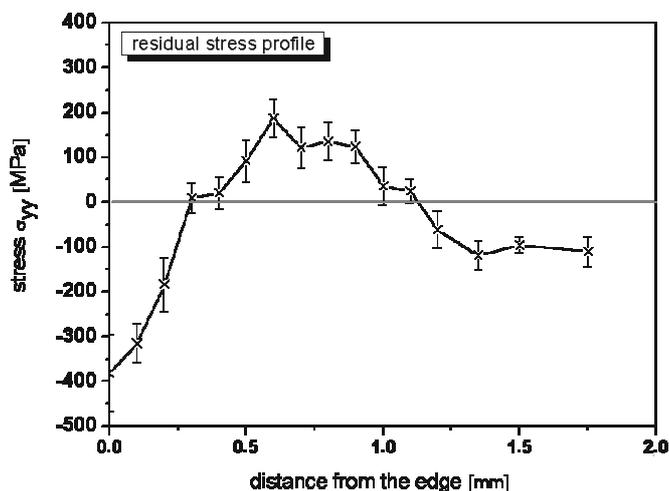

Fig. 19. Experimentally determined residual stresses in y-direction σ_{yy}^{res} at the side area as a function of the distance from the edge after a complete loading-unloading cycle with a maximum compression load of 60 kN

4. Summary

A combined experimental and numerical approach was applied to develop a basic understanding of the fatigue damage process taking place at edges exposed to cyclic mechanical loads.

For the physical simulation a recently developed cyclic edge-loading test was used in order to simulate the fatigue loading of the edges of manufacturing tools. This test was specially designed to investigate the damage phenomena at the loaded edges and to study the local strain distribution, the formation of microcracks, and the nucleation and growth of fatigue cracks by means of microscopic methods. The investigated material was the powder metallurgically produced tool steel S390 MICROCLEAN with a hardness of 62 HRC.

The results indicate strain localisation in deformation bands; one deformation band forms at the edge inclined about $45°$ to the loading direction and a second band forms in a quadrant shaped zone that encompasses the higher strain region from the lower strain region. Cyclic plastic straining mainly occurs in the first few cycles. Overall plastic deformation stops after a few cycles but local plastic deformation is still prevalent and causes ongoing damage at the microscale. Damage mainly occurs by microcrack formation caused by cracking of primary carbides or carbide clusters or by void formation due to debonding of carbides from the metallic matrix. Optical strain measurements revealed inhomogeneous deformation of the tool steel leading to higher strained regions embedded in regions with lower strains. In most cases only one fatigue crack is formed at the transition region from the extensively strained to the lower strained region at the side area. The main reason for the formation of the fatigue crack at this position is the early nucleation of cracks due to breaking of carbides or due to deformation bands on the one hand, and the existence of tensile residual stresses on the other.

Finite element calculations were performed in order to provide a better understanding of the loading conditions at edges subjected to cyclic mechanical loads. A comparison of the numerical simulation results with the experimental results revealed good accordance. For instance, the numerical simulation predicts similar strain distribution pattern as they were found in the experiments and there is also a good accordance with the experimentally determined residual stress distribution at the side area. The simulation results indicate that cyclic softening may be responsible for the localisation of plastic strain in strain bands. It can be concluded that the numerical simulation gives a valuable insight to the further local loading conditions but it has to be taken into account that not all phenomena can be described in detail, e.g. only mean strains can be predicted but the inhomogeneous strain distribution cannot be considered.

REFERENCES

[1] H. Chandrasekaran, S. Svensson, and M. Nissel, "Tool chipping during power hack sawing and the role of saw material characteristics", *Ann. CIRP* 36 (1), 27–31 (1987).

[2] D. Gamby, C. Henaff-Gardin, and M.C. Lafarie-Frenat, "Propagation of edge cracking towards the centre of laminated composite plates subjected to fatigue loading", *Composite Structures* 56 (2), 183–190 (2002).

[3] V. Leskovšek, B. Ule, A. Rodič, and D. Lazar, "Optimization of vacuum heat treatment of cutting dies made from HSSM2 (AISI)", *Vacuum* 43 (5–7), 713–716 (1992).

[4] M.T. Hanson and L.M. Keer, "Analysis of edge effects on rail-wheel contact", *Wear* 144 (1–2), 39–55 (1991).

[5] P.J. Gruber, W. Ecker, M. Krobath, S. Marsoner, G. Jesner, R. Ebner, and O. Kolednik, "Loading conditions and damage evolution near the edge of a stamping tool-new experiments and numerical simulations", *Proc. Tool 09 – Tool Steels Conf.* 1, CD-ROM (2009).

[6] P.J. Gruber, G. Jesner, R. Ebner, and O. Kolednik, "High-strength steel under monotonic and cyclic loading – a study on damage evolution near the edge of a stamping tool", *BHM* 154 (5), 205–210 (2009).

[7] *Internal report at MCL*, (2008).

[8] B. Griffiths, "Manufacturing surface technology - surface integrity and functional performance", *Manufacturing Engineering Modular Series* 1, CD-ROM (2001).

[9] P.J. Gruber, "Characterisation of the behaviour of high-strength tool steel edges under cyclic loading", *PhD Thesis*, University of Leoben, Leoben, 2010.

[10] T.L. Anderson, *Fracture mechanics – Fundamentals and applications*, CRC Press Taylor & Francis Group, Boca Raton, 2005.

[11] J.L. Chaboche, "Continuous damage mechanics – A tool to describe phenomena before crack initiation", *Nuclear Engineering and Design* 64, 233–247 (1981).

[12] W. Ecker, M. Leindl, T. Antretter, R. Ebner, I. Siller, and S. Nissle, "Effect of material properties on the thermo-mechanical loading and damage of pressure casting dies – a numerical study", *Proc. Tool 09 – Tool Steels Conf.* 1, CD-ROM (2009).

[13] C. Genzel, C. Stock, and W. Reimers, "Application of energy-dispersive diffraction to the analysis of multiaxial residual stress fields in the intermediate zone between surface and volume", *Materials Science and Engineering* 372 (1–2), 28–43 (2004).

[14] S. Suresh, A. Mortensen, and A. Needleman, *Fundamentals of Metal Matrix Composites*, Butterworth – Heinemann, New York, 1993.

[15] S. Suresh, *Fatigue of Materials*, Cambridge University Press, Cambridge, 1998.

[16] T. Wehner and A. Fatemi, "Effects of mean stress on fatigue behaviour of a hardened carbon steel", *Int. J. Fatigue* 13 (3), 241–248 (1991).

[17] N.A. Fleck, C.S. Shin, and R.A. Smith, "Fatigue crack growth under compressive loading", *Engineering Fracture Mechanics* 12 (1), 173–185 (1985).

[18] W. Ecker, "Modeling of the thermo-mechanical behaviour of pressure casting dies"; *PhD Thesis*, University of Leoben, Leoben, 2008.

[19] G. Jesner, S. Marsoner, I. Schemmel, K. Haeussler, and R. Ebner, "Damage mechanisms in materials for cold forging dies under loading conditions typical for dies", *Int. J. Microstructure and Materials Properties* 3 (2/3), 297–310 (2008).

[20] G. Trattnig, T. Antretter, and R. Pippan, "Fracture of austenitic steel subject to a wide range of stress triaxiality ratios and crack deformation modes", *Engineering Fracture Mechanics* 75 (2), 223–235 (2008).

[21] D.L. Davidson, "The observation and measurement of displacements and strain by stereoimaging", *Scanning Electron Microscopy* 11, 79–86 (1979).

[22] A. Tatschl and O. Kolednik, "On the experimental characterization of crystal plasticity in polycrystals", *Materials Science and Engineering* A 342, 152–168 (2003).

[23] A. Tatschl and O. Kolednik, "A new tool for the experimental characterization of micro-plasticity", *Materials Science and Engineering* A 339, 115–122 (2003).

[24] K. Unterweger and O. Kolednik, "The local deformation behaviour of MMCs – an experimental study", Z. Metallkunde 96, 1063–1068 (2005).

[25] I.C. Noyan and J.B. Cohen, *Residual Stress Measurement by Diffraction and Interpretation*, Springer-Verlag, Berlin, 1987.

[26] *Realistic Simulation Solutions*, www.simulia.com.

[27] J.L. Chaboche, "Constitutive equations for cyclic plasticity and cyclic viscoplasticity", Int. J. Plasticity 5, 247–302 (1989).

[28] J. Lemaitre and J.L. Chaboche, *Mechanics of Solid Materials*, Cambridge University Press, Cambridge, 1990.